Transport mechanism of lithium ions in non-coordinating P(VdF-HFP) copolymer matrix

Lena Mathies[a], Diddo Diddens[b], Dengpan Dong[c], Dmitry Bedrov[c], Hartmut Leipner[a]

[a] *Interdisziplinäres Zentrum für Materialwissenschaften, Martin-Luther-Universität Halle-Wittenberg, Heinrich-Damerow-Str. 4, 06120 Halle*
[b] *Helmholtz-Institute Münster: Ionics in Energy Storage (IEK-12), Forschungszentrum Jülich GmbH, Corrensstraße 46, 48149 Münster, Germany*
[c] *Department of Materials Science & Engineering, University of Utah, 122 South Central Campus Drive, Salt Lake City, Utah 84112, USA*

Abstract

Polymer films based on poly(vinylidene difluoride-co-hexafluoropropylene) (P(VdF-HFP)) with different amounts of bis(trifluoromethane)sulfonimide lithium salt (LiTfSI) were prepared from acetone solution in a doctor blade casting machine under controlled and reproducible drying conditions.

The modification of the copolymer-based layers show a significant enhancement of conductivity over several orders of magnitude for increasing LiTfSI content and a constantly low electronic conductivity. The addition of salt results in a structural change of the crystalline areas in the semi-crystalline copolymer matrix from α- to γ-phase of P(VdF), which has been studied using Raman spectroscopy and X-Ray diffraction. Lithium ions are coordinated by oxygen atoms of $TfSI^-$ as verified by Raman spectroscopy and molecular dynamics simulations. Based on the experimental data and simulation results, we propose a transport mechanism for the lithium ions through salt channels in the amorphous regions of the non-coordinating copolymer matrix via hopping between stabilized positions.

Email addresses: `lena.kuske@cmat.uni-halle.de` (Lena Mathies), `d.diddens@fz-juelich.de` (Diddo Diddens), `cherrydons@hotmail.com` (Dengpan Dong), `d.bedrov@utah.edu` (Dmitry Bedrov), `hartmut.leipner@cmat.uni-halle.de` (Hartmut Leipner)

Keywords: Polymer electrolyte, LiTfSI, P(VdF-HFP), transport mechanism, MD simulation

1. Introduction

Energy storage devices are highly demanded and therefore in focus of recent investigation. Among the common battery systems, Li ion batteries show the highest energy density and dominate todays energy storage market. Most rechargeable Li ion batteries still use liquid electrolytes due to the high ion conductivity. Generally they are based on organic alkyl carbonates and thus highly volatile and flammable. Beside the risk of leakage, liquid electrolytes show a reactivity towards Li metal, and the formation of dendrites can result in internal short circuits destroying the battery.

Polymer based electrolyte materials have been intensively studied during the last decades to replace liquid electrolytes [1]. They can be seen as a hybrid material between solid state and liquid electrolyte materials and offer good mechanical stability, low flammability, easy processablity, high tolerance to shocks or vibration, and good interfacial contact and compatibility with different electrode materials. There are three common ways to modify the properties of polymer-based matrices for the application as electrolyte layer in Li ion batteries: (i) In polymer electrolytes (PE), an inorganic Li salt is solvated in an organic polymer containing electron donating groups that directly interact with the Li cation [2, 3]; (ii) in gel polymer electrolytes (GPE), the Li salt is mixed with a plasticizer including carbonates, ethers or ionic liquids, and combined with a porous polymer matrix to form a flexible free standing film containing the electrolyte solution [4, 5]; (iii) in composite materials, a polymer matrix is actively or passively modified by adding a Li ion conducting or non-conducting nanosized filler material, respectively [6, 7, 8]. These strategies and the combination of the different approaches led to ion conductivities for polymer based electrolytes in the range of mS/cm [9], competing with liquid electrolytes, but

often still lacking the desired thermal or electrochemical stability and showing small Li ion transference numbers [1].

The polymer P(VdF) provides excellent mechanical and thermal stability, is chemically inert, stable in cathodic environment and has a low permittivity and electron conductivity [10]. The most important crystalline phases of P(VdF) are the non-polar α-phase with a TGTG$^-$ (*trans*, *gauche*, *trans*, minus *gauche*) chain conformation (form II) and the polar β- and γ-phase (form I and III), consisting of only trans and TTTGTTTG$^-$ chain conformation, respectively [11]. The copolymer P(VdF-HFP) shows reduced crystallinity, better solubility in different solvents even at room temperature compared to the pure polymer, and forms free standing films for HFP contents up to 25 % [12]. The semi crystalline copolymer matrix of P(VdF-HFP) consists of crystalline areas formed by crystallized P(VdF) units [13], while HFP enlarges the inter chain distance due to the bulky CF_3 group and increases the amorphous fraction in the matrix.

P(VdF-HFP) is a non-coordinating polymer, that does not have any atomic groups that are known to interact directly with the Li cations. This is a fundamental difference to the intensively studied PEO–lithium salt systems, where a direct localization of the Li ions is promoted through the electron donating oxygen atoms in the chains of the polymer [14]. P(VdF-HFP) is often studied for GPE, where ionic liquids are used [15] or the Li salt is dissolved in e. g. in propylene carbonat and/or diethyl carbonate [10], and the conductivity has been explained by the formation of a gel within a free standing copolymer matrix [16, 17].

Bis(trifluoromethane)sulfonimide lithium salt (LiTfSI) provides an excellent solubility in many solvents, is chemically and thermally stable and used in many electrolyte liquids or ionic liquids due to the large and flexible anion with extensive charge delocalization [18].

Different studies present P(VdF-HFP) based electrolyte membranes with similar salts but additional fillers [19, 20] and for P(VdF-HFP)-LiTfSI films without additional fillers conductivities of 0.1 mS/cm were reached [21]. Still the conduction mechanism is not understood in detail. In this study we show a

conductivity enhanced over several orders of magnitude of P(VdF-HFP)-based electrolyte films with up to 25 wt-% LiTfSI. Besides the electrical properties, the structural changes provoked through the addition of salt are investigated, using experiments and atomistic molecular dynamics simulations, and a conductivity mechanism is proposed to explain the increase of conductivity upon addition of salt.

2. Experimental

2.1. Material Preparation

The copolymer P(VdF-HFP) with a HFP content of 5 wt% from Sigma Aldrich and acetone from Micro Chemicals were used as received. LiTfSI from Alfa Aesar was dried under vacuum for 24 h at 120 °C before use. For the solutions, P(VdF-HFP) and LiTfSI were mixed with acetone in the desired weight ratios and stirred at room temperature until the copolymer and salt totally dissolved. The solutions were cast on aluminium substrates in a doctor blade casting machine under controlled drying conditions. The heatable process table was set to room temperature. The drying stage equipped with an infrared lamp and a convection dryer was set to low intensity(250 W) and 25°C, respectively, to ensure the formation of uniform, dense films of a well defined thickness of approximately 6-7 μm for a single layer. Investigations presented here are done with samples composed of three layers subsequently coated on top of each other resulting in a final thickness of 18-20 μm.

2.2. Electrical Characterization

Electrical measurements were performed at room temperature using a Metrohm Autolab PGSTAT128N potentiostat equipped with an additional impedance analyzer and Autolab Nova software. Circular samples were fixed in a Swagelok cell between two Li ion blocking electrodes made of stainless steel with a diameter of 10 mm. For the DC polarization measurements samples were put under

a fixed voltage of 500 mV, and the current through the sample was measured and tracked over time. The conductivity

$$\sigma = \frac{l \cdot I}{A \cdot U},$$

with l being the thickness of the sample, A the area of the electrodes and I and U the measured current and set voltage, respectively, was plotted over time. The electron conductivity was extracted by fitting the converged value after several minutes, when any mobile charged carriers had moved to the electrodes and only electrons are contributing to the current flow.

Impedance measurements were performed in a frequency range of 10^6 - 10^{-2} Hz with a voltage amplitude of 100 mV between two stainless steel electrodes with a diameter of 10 mm. All impedance measurements were evaluated frequency dependent according to the dielectric spectroscopy school [22]. The real part of the conductivity (σ') can be calculated from the measured complex impedance, its real and imaginary part (Z^*, Z' and Z'', respectively and $Z = \sqrt{Z'^2 + Z''^2}$) according to

$$\sigma' = \frac{l}{A} \frac{Z'}{|Z|^2}$$

It is a measure for the flow of charges and plotting against the frequency f in a double logarithmic plot, the conductivity of the sample (σ_{DC}) can be extracted. The impedance data were evaluated according to the detailed description of Chan *et al.* [23, 24] and is described in the supplementary information in detail (Figure 9).

Temperature dependent measurements were done with two distinct samples in a temperature range of 150 - 450 K in a frequency window of 10^6 - 10^{-2} Hz on a high resolution α-analyser from Novocontrol Technologies GmbH & Co. KG. A Quatro temperature controller ensured a thermal stability of $\leq$1 K. Samples were measured between two brass electrodes with a diameter of 10 mm.

2.3. Structural Characterization

For structural analysis approximately 1 cm^2 big pieces of the samples were measured at different positions in a Dilor LabRam Raman microscope equipped with a 632.8 nm HeNe-laser (30 mW) and a 100-fold magnification lens. X-ray diffractometry (XRD) was done in transmission mode with a STOE-multipurpose diffractometer system type STADI MP, with a MYTHEN1K detector and $Mo_{K\alpha}$ irradiation ($\lambda = 0.7093$ Å). Scanning electron microscopy (SEM) was performed with a XL30 ESEM FEG taking secondary electron (SE) images of the surfaces.

2.4. Molecular Dynamics Simulations

The molecular dynamics (MD) simulations have been performed with the simulation code *Lucretius* developed at the University of Utah using the APPLE&P polarizable force field [25, 26]. The P(VdF-HFP) polymer chains were composed of a PVdF and a PHFP block with ten monomers each (see Figure 11 in the Supplementary Information (SI)), and the following systems were created using these polymers: 1). 64 P(VdF-HFP) chains with 64 LiTfSI ion pairs, 2). 32 P(VdF-HFP) chains with 64 LiTfSI ion pairs, 3). 40 P(VdF-HFP) chains with 128 LiTfSI ion pairs, 4). 24 P(VdF-HFP) chains with 128 LiTfSI ion pairs, corresponding to 12, 21, 30, and 42 wt.-% LiTfSI.

Increasing amounts of salt were intended to mimic the local enrichment of LiTfSI in the amorphous domains of the polymer electrolyte and observe structural changes that might explain the experimentally determined rise of conductivity.

The initial systems were compressed to the target density during 30 ps, and equilibrated subsequently for at least 16 ns in the NpT ensemble, followed by subsequent production runs of $300 - 530$ ns in the NpT ensemble at 363 K. Both the temperature and the pressure of the system were maintained by a Nosé-Hoover chain thermostat (coupling frequency 0.01 fs^{-1}) and barostat (coupling frequency 0.0005 fs^{-1}) [27], while periodic boundary conditions were applied in all three dimensions. Electrostatic interactions have been treated by the Ewald summation technique with a cut-off radius of 15 Å, an inverse Gaussian

charge width of $0.23\,\text{Å}^{-1}$, and $7 \times 7 \times 7$ vectors for the summation in reciprocal space. Van-der-Waals interactions have been truncated at 15 Å, beyond which a continuum-model dispersion correction was applied. All bonds were constrained by the SHAKE algorithm [28, 29]. A multiple-time-step integration scheme [30, 31] was used to integrate the equations of motion, where a time step of 0.5 fs has been used for bonds and angles, respectively. For torsions and non-bonded interactions up to a distance of 8 Å, a time step of 1.5 fs was used, and finally, for non-bonded interactions between atoms separated more than 8 Å, and the reciprocal part of the Ewald summation, a time step of 3 fs was used. The induced dipoles were determined iteratively where the corresponding dipole-dipole interactions were scaled to zero by a tapering function between 14.5 and 15 Å. Note that unlike the experimental samples, the polymer in the simulations was fully amorphous, as crystallization effects are typically not observed in MD simulations due to the rather short time scales that can be accessed (i.e. $10^2 - 10^3$ ns), unless the system is prepared in the crystalline state.

3. Results and Discussion

3.1. Material Preparation

The preparation process presented from acetone solutions under controlled drying conditions at ambient air and room temperature, led to free standing films with a uniform and dense morphology and fine surface structure (cf. representative picture and SEM image of a pure P(VdF-HFP) film in Figure 1). The dried films showed no indication of residual solvent and also additional drying at higher temperatures over night does not affect the development of the conductivity based on the addition of LiTfSI discussed here. See supplementary information for more details (text and Figures 7, 8). The addition of LiTfSI had no impact on the morphology and surface structure of the films. The reproducible drying conditions and the non-toxic solvent used for the process are suitable for up scaling in an industrial way, which is desired in the view of

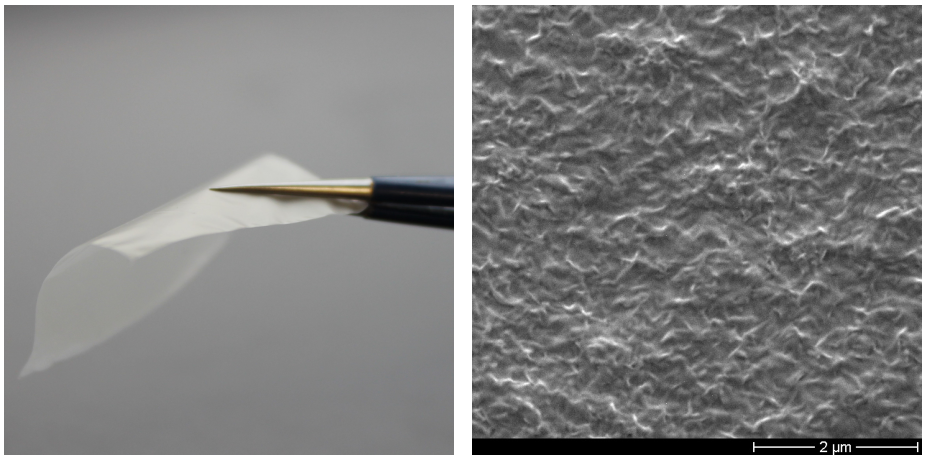

(a) (b)

Figure 1: Free standing films; (a) photograph and (b) secondary electron image (SEM) of a pure P(VdF-HFP) film with a thickness of 20 μm.

commercially processable materials for electronic devices like batteries.

3.2. Electrical Properties

While lithium ion transport in PEO based systems is well studied [2, 14, 32, 33], the conduction mechanism in solid polymer systems based on P(VdF-HFP) is not fully understood. The insight and understanding of the transport mechanism in this non-coordinating copolymer matrix is crucial for further investigations of non-coordinating polymers for electronic devices like lithium ion batteries, with the aim of a high Li^+ conductivity, combined with the chemical and thermal stability of the matrix material against Li metal, potentially used as anode material in lithium ion batteries.

In Figure 2 the total conductivity from impedance measurements as well as the electron conductivity extracted from DC polarization measurements are plotted against the salt content of the samples. There is a dispersion of the measured conductivity values over the measurements of different samples with

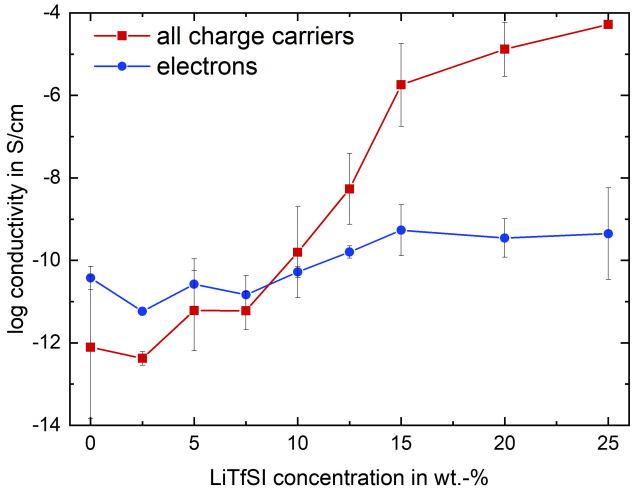

Figure 2: Conductivities of the electrolyte films at room temperature in dependence of the LiTfSI concentration added to the pure copolymer solutions with the standard deviation over several measurements of different samples with same composition; red squares = conductivities extracted from impedance measurements, blue circles = electron conductivities measured with the DC polarization method.

the same composition, illustrated by the error bars. Despite the standard deviation the total conductivity of the samples show a strong dependence on the salt concentration and conductivity was enhanced over several orders of magnitude while electron conductivity remains low.

Samples with less than 10 wt.-% LiTfSI show a low conductivity probably dominated by electrons as charge carriers. In samples with more than 10 wt.-% LiTfSI the conductivity is enhanced over five orders of magnitude, while the electron conductivity is staying in the range of 10^{-10} S/cm, indicating that electron conductivity is not playing a minor role in these samples. The strong increase of the conductivity with addition of salt suggests that higher amounts of salt ions or agglomerates are mobile in the copolymer matrix contributing to the conductivity.

To estimate the contribution of lithium ions to the total charge flow we measured lithium ion transference numbers ($t_{Li^+} = 0.47$) and calculated lithium

ion transport numbers ($T_{Li^+} \approx 0.5$). See the supplementary information for measurement and calculation details and a discussion on the validity for the determined values for the herein investigated material system. Our finding of ≈ 0.5 indicates that both ion species contribute to the overall charge transport. In the following, we elucidate how the salt ions are coordinated to subsequently discuss the transport mechanism in more detail.

3.3. Structural Properties

P(VdF-HFP) forms a semi-crystalline copolymer film, with P(VdF) units forming the crystalline areas within the amorphous copolymer matrix. The pure copolymer film shows a low degree of crystallinity and the positions of the signals reveal the formation of α-phase of P(VdF) (cf. XRD patterns in Figure 3a with marked reflex positions for the different P(VdF)-phases [34]). With the addition of salt the signal to noise ratio and the intensity of the signal at 8.5° is reduced, indicating a lower degree of crystallinity and a change of structure in the crystalline areas of the copolymer films, respectively.

According to Raman spectroscopy, the crystalline areas in the pure P(VdF-HFP) films consist of α-phase (form II) of P(VdF) with a TGTG$^-$ chain conformation and a polar unit cell. In Figure 3c, the Raman measurements of pure P(VdF-HFP) and films with different LiTfSI contents are shown. For better comparison the spectra are normalized. The spectrum of the pure copolymer film shows all relevant bands of the α-phase of P(VdF) with the expected relative intensities [35]. The characteristic bands belonging to the crystalline α-phase of P(VdF) decrease or shift with the addition of salt. In Figure 3b the bands in the range of $800\,\mathrm{cm}^{-1}$ are shown in more detail for samples containing 0, 5, 10 and 25 wt% LiTfSI. With increasing salt concentration the band at $800\,\mathrm{cm}^{-1}$ is broadening and strongly decreasing, while bands at 815, 830 and $840\,\mathrm{cm}^{-1}$ get much stronger. The signal at $800\,\mathrm{cm}^{-1}$ results from CH_2 rocking vibrations in the α-phase of P(VdF). With the addition of salt the electrostatic environment in the copolymer films is changed and the surrounding of Raman active bonds

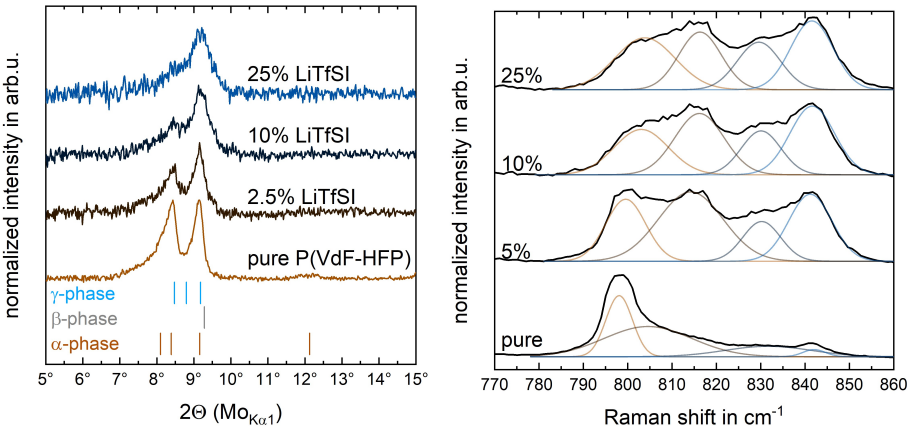

(a)

(b)

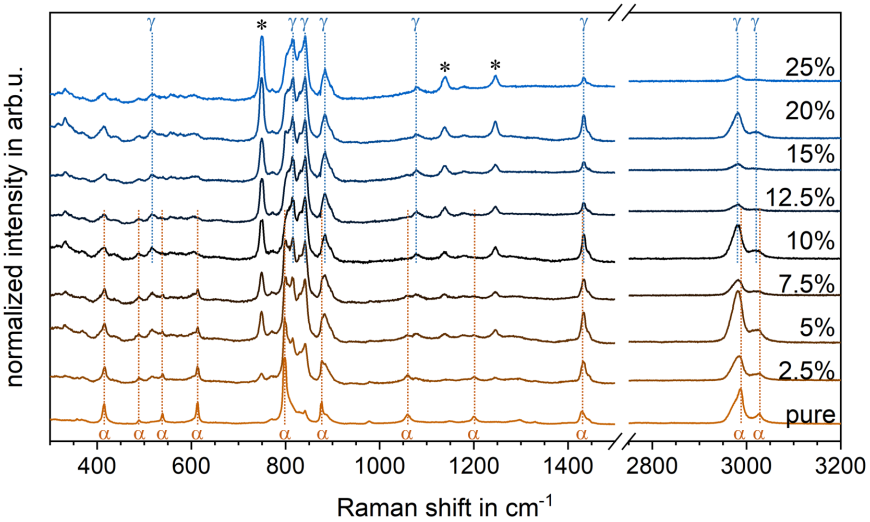

(c)

Figure 3: Structural characterization of the polymer electrolyte films; (a) XRD of films with different LiTfSI concentrations and pure P(VdF-HFP) with the expected positions for the different crystalline phases of P(VdF) [34]. (b) Detailed Raman spectra of films with different LiTfSI concentrations and pure P(VdF-HFP); the distinct band of α-phase at $800\,\mathrm{cm}^{-1}$ decreases, while bands at 815, 830 and $840\,\mathrm{cm}^{-1}$ characteristic for the γ-phase increase. (c) Overview Raman spectra. Distinct bands of LiTfSI are marked with an asterix; the characteristic bands of the α-phase of P(VdF) in the pure P(VdF-HFP) film are marked with α, characteristic γ-phase bands arising with the addition of salt are marked with γ.

varies, resulting in a broadening of the characteristic α-phase bands. According to different calculations and experimental studies [35, 34, 36] the band at 840 cm^{-1} results from CH_2 rocking and CF_2 asymmetric stretching modes and is pronounced strongly in samples containing the polar γ-phase of P(VdF) with a $TTTGTTTG^-$ chain conformation. Bands at 812 and 833 cm^{-1} are also attributed to the γ-phase [34]. Tashiro *et al.* asigne the band at 811 cm^{-1} to CH_2 rocking modes in the γ-phase with TTTG chain conformation [37]. Characteristic α-phase bands at 876, 1058, 1430, 2990 and 3030 cm^{-1} are shifting towards 884, 1078, 1434, 2980 and 3020 cm^{-1}, respectively with the addition of LiTfSI (see Figure 3c). Bands at wavenumbers 884 and 1434 cm^{-1} are exclusively characteristic for the γ-phase, while the other bands shift to values that could be related to ether the γ- or the highly polar β-phase of P(VdF) with an all trans zigzag chain conformation. Reference values are taken from calculations and experimental results from Kobayashi *et. al* [35].

The evaluation of the peak shifts as well as the change in intensities lead to the conclusion that the addition of the polar Li salt promotes the formation of the polar γ-phase in the crystalline areas of the semicrystalline copolymer films, although the α-phase is kinetically favoured [38]. Despite the formation of the crystalline γ-phase of P(VdF), there is no further relevant change in the Raman spectra indicating that the salt is mainly solvated in the amorphous areas.

3.4. Conduction Mechanism

It has been shown that the addition of HFP monomers reduces the crystallinity in the PVdF polymer matrix [12]. As the copolymer chain of HFP has the same functional CF_3 groups that are also present in the bulky $TfSI^-$, the salt anions could interact with the polymer matrix in the same way the functional CF_3 side of HFP is doing. Raman spectra and XRD measurements show slightly lower intensities for samples with higher salt concentrations indicating that there is less crystalline phase. Raman spectra show no significant change in peak width for increasing salt concentration, suggesting that the salt accumu-

lates in the amorphous phase and does not interact much with the crystalline areas of the semi-crystalline copolymer matrix.

In the Raman spectra of Figure 3c, new distinct peaks appear that are characteristic for the TfSI anion of the Li salt. The band at approximately $750\,\mathrm{cm}^{-1}$ arises from expansion and contraction of the whole anion ($TfSI^-$) while the band at $1245\,\mathrm{cm}^{-1}$ is attributed to S-C and C-F stretching modes [18]. Seo *et al.* studied thoroughly different possible solvation states of LiTfSI in different media and evaluated Raman spectra as well as XRD for a detailed analysis of the different structures and coordinations of the diluted salt [18]. The location of the bands in our samples (749.5 and $1245.6\,\mathrm{cm}^{-1}$) reveals that the salt is neither dissolved into separated ion pairs nor contact ion pairs. It rather forms aggregates, where Li^+ is coordinated through oxygen atoms of the sulfonyl groups of different $TfSI^-$ anions, in a similar way to the coordination in the pure salts crystal structure [39]. Similar coordination of Li^+ in a LiTfSI-carbonate solution was detected by McOwen *et al.* [40] analyzing Raman measurements. As there are no direct interaction sides in the copolymer chains, like e.g. oxygen atoms in PEO, a direct interaction of Li^+ and the P(VdF-HFP) copolymer matrix is not expected. However a significant enhancement of the conductivity was seen upon addition of lithium salt and charge carriers, e.g. ions or salt clusters, are mobile in the P(VdF-HFP) copolymer matrix at higher salt concentrations. Li^+ is coordinated to oxygen atoms of the sylfonyl groups of $TfSI^-$ and the added salt forms aggregates. At higher salt concentrations the salt clusters could form a percolating network and the Li^+ possibly moves through $TfSI^-$ channels hopping from one stabilized position to the next. In liquid electrolytes similar hopping mechanisms for lithium ions stabilized by oxygen atoms of sylfonyl groups was presented by Dokko *et al.* [41].

The proposed conduction mechanism for lithium ions in the P(VdF-HFP)-LiTfSI films is shown in Figure 4a. At high salt concentrations the P(VdF-HFP)-LiTfSI system could be compared to the polymer-in-salt regime of systems based on coordinating polymers. In these systems the dominating transport mechanism for lithium ions changes for high salt concentrations, when entering

the polymer-in-salt regime, and the coordination of Li^+ through the polymer plays a minor role [42]. Salt clusters percolate [43] and conductivity is explained based on the knowledge of ionic liquids, where exchange of anions in the first coordination shell is suggested to be the dominating mechanism for lithium ion transport [44]. The same local relaxation also contributes to the anionic motion (cf. section 3.5).

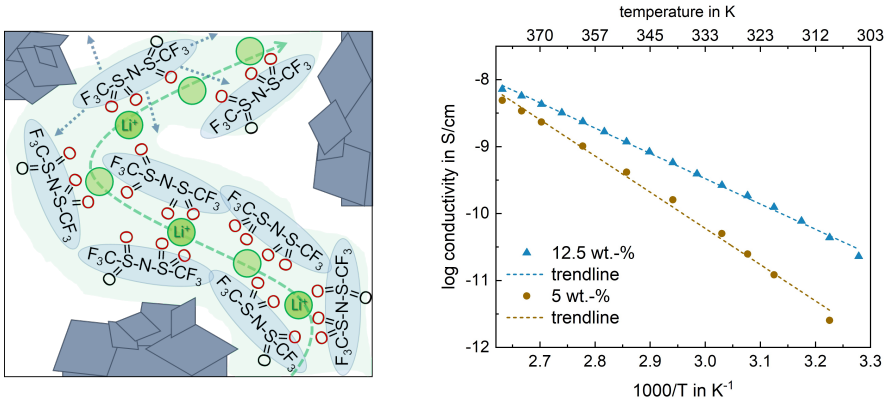

(a) (b)

Figure 4: (a) Suggested mechanism of the ion transport; grey: crystalline areas, green: stabilized positions for Li^+ ions, red O: interacting oxygen atoms of sylfonyl groups of $TfSI^-$. Lithium ions move via hopping from one $TfSI^-$ stabilized position to the next, their pathway is indicated by the green dashed arrow, while the blue dotted arrows indicate the possible motion for a $TfSI^-$ enabled by local relaxation (b) Arrhenius plot for the first heating cycle for two different salt concentrations.

To gain further insight into the conduction mechanism, temperature dependent AC-measurements of two samples with low (5 wt.-%) and high (12.5 wt.-%) LiTfSI concentrations have been evaluated. The measurements were done at a different measurement set-up, with a different electrode material and the values for conductivity are differing from the measurements presented in Figure 2. For the higher concentration the value is outside of the determined standard deviation. Still the course of the two measurements for high and low salt show distinct courses in the Arrhenius plot (cf. Figure 4b) and give additional

information about the conduction mechanism. The slope is lower for higher salt concentration, attributed to the fact that there are more anions and much shorter distances between the $TfSI^-$ stabilized positions, leading to a lower activation energy for Li^+ to jump from one stabilized position to the next. An Arrhenius like behaviour can be seen. The percolating clusters form a salt network allowing lithium ions to hop from one stabilized position to the next within the channels throughout the copolymer matrix. For the lower salt concentration the data show a deviation from the linear trend, indicating that polymer chain motion might be relevant for the conduction mechanism, resulting in a Vogel-Tammann-Fulcher law dependence [45]. Conductivity at low salt concentration could be explained by salt clusters moving through the copolymer film, strongly depending on free volume in the matrix generated by segmental motion of copolymer chains. Electron conduction can not be neglected in the sample with low LiTfSI concentration and might also influence the change in conductivity with increasing temperature. P(VdF-HFP) is a thermoplast with a negligible intrinsic electronic conductivity and electrons in our samples may predominantly move via hopping mechanism through defects and impurities in the polymer matrix, faciliated by increasing temperature due to segmental motion [46]. For further cooling/heating cycles the two different samples show exactly the same course in Arrhenius plots, differing from the first heating cycle. The samples seem to change after being heated and possibly degenerate due to melting and recrystallization processes in the films.

For samples with a high salt concentration the temperature dependent data underline the proposed conduction mechanism through $TfSI^-$ stabilized positions in salt channels in the amorphous phase of the copolymer matrix. A percolating network of salt clusters provide pathways for Li^+, that is coordinated by different oxygen atoms of sulfonyl groups of different $TfSI^-$ anions (cf. Figure 4a).

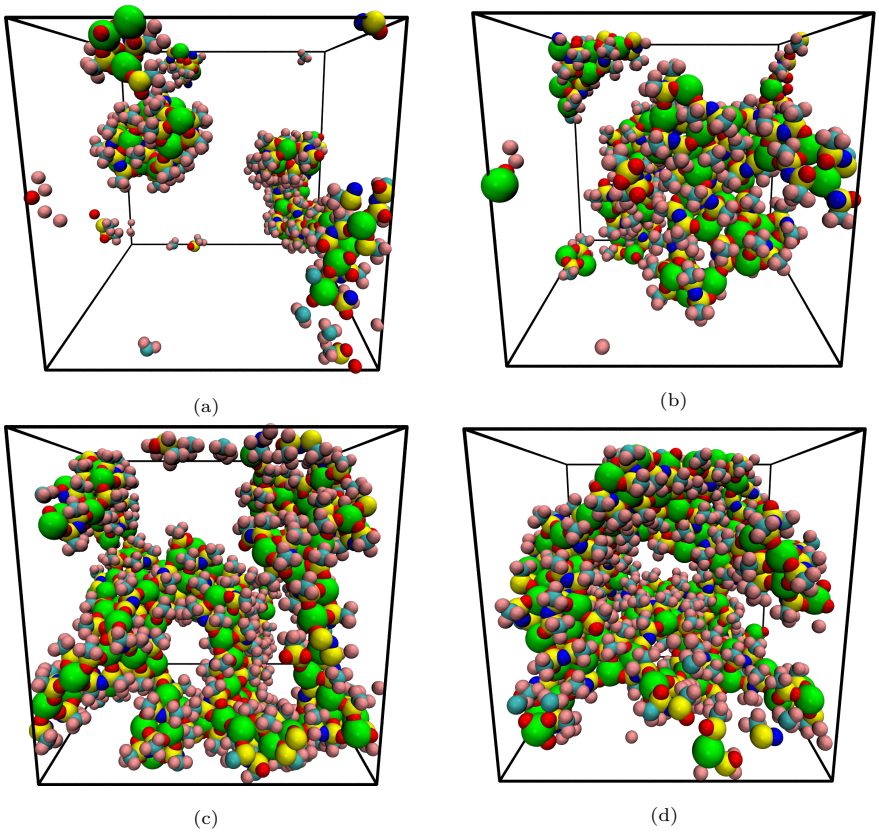

Figure 5: Snapshots from the MD simulations for the individual LiTfSI concentrations of (a) 12, (b) 21, (c) 30, and (d) 42 wt% LiTfSI. Polymer atoms: invisible, lithium: green, carbon: cyan, nitrogen: blue, oxygen: red, fluorine: pink, sulphur: yellow.

To further support our experimental findings, we performed MD simulations of the amorphous domains of the electrolyte. Figure 5 shows snapshots of the ion aggregates obtained from the molecular dynamics (MD) simulations for the individual concentrations. For better clarity, polymer atoms are invisible. We observe that for the lower concentrations (Figure 5a and 5b), isolated ion clusters are forming, which would not allow for long-ranged macroscopic transport of ions and thus any significant ionic conductivity in the experiments. However, the Raman data suggests that LiTfSI preferentially accumulates in the amor-

phous domains of the polymer (cf. sketch in Figure 4a), resulting in locally increased LiTfSI concentrations. Motivated by these experimental findings, we thus also simulated the amorphous polymer region with larger concentrations of 30 and 42 wt% LiTfSI (Figure 5c and 5d). For these concentrations, we mainly find percolating LiTfSI clusters that are compatible with macroscopic ion transport (see below).

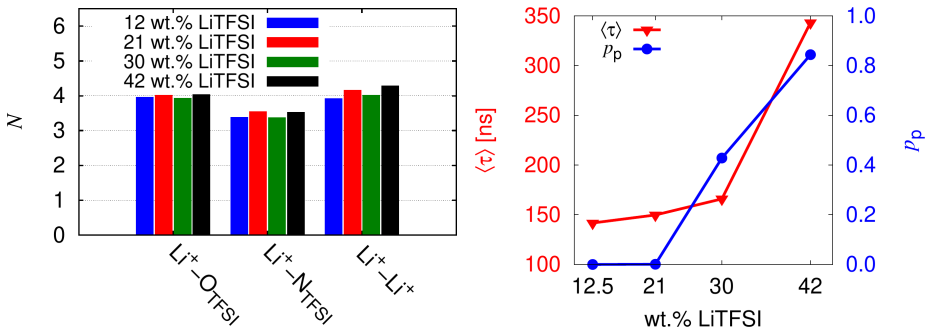

(a) (b)

Figure 6: (a) Coordination numbers of the lithium ions in the MD simulations and (b) average coordination times $\langle\tau\rangle$ between Li^+ and TfSI (red curve) as well as the probability p_p that the LiTfSI clusters are percolating throughout the entire simulation box (blue curve).

Figure 6a shows the coordination numbers between lithium ions and oxygen atoms of TfSI (Li^+-O_{TfSI}), lithium ions and nitrogen atoms of TfSI (Li^+-N_{TfSI}), as well as two distinct lithium ions (Li^+-Li^+) for the different concentrations. The coordination numbers were derived from the volume integral over the first coordination peak of the radial distribution functions shown in Figure 12 in the SI. The size of the first coordination sphere was defined as the distance for which the first minimum after the first coordination peak occurred in the RDF, leading to cut-off distances of 2.8, 5.2 and 6.9 Å for Li^+-O_{TfSI}, Li^+-N_{TfSI}, and Li^+-Li^+, respectively. These values were chosen irrespective of the LiTfSI concentration, as we found that the peak positions remained unaffected (Figure 12 in SI).

From Figure 6a we note that Li^+ is on average coordinated by four oxygen atoms of TfSI independent of the salt concentration. At the same time, $3-4$

TfSI nitrogen atoms are present in the vicinity of a given lithium ion, indicating that most of the four coordinating TfSI oxygen atoms originate from distinct TfSI ions, and that the bidenate coordination of a single TfSI ion [47, 48, 49] is only encountered for a minor fraction of TfSI. Finally, we also observe that each lithium ion is surrounded by about four other lithium ions up to a distance of about 7 Å, which is again independent of the LiTfSI concentration. Furthermore, we note that there is no pronounced coordination between Li^+ or fluorine atoms of TfSI and the fluorine atoms of the copolymer for both the PVdF and the PHFP moieties (see Figure 13 in SI). In total, these findings perfectly support the microscopic picture sketched in Figure 4a, in which LiTfSI clusters form in the amorphous domain of the copolymer host, as also observed from Figure 5.

Figure 6b shows the average residence time $\langle\tau\rangle$ that a coordinating TfSI anion around a given lithium ion spends in its first coordination shell (red curve, see details of the calculation and Figure 14 in the SI). We observe that up to 30 wt% LiTfSI, $\langle\tau\rangle$ is about 150 ns and only marginally increases with the LiTfSI concentration, suggesting that the local dynamics within the ion cluster is essentially insensitive to the salt concentration. For 42 wt% LiTfSI, we find a steeper increase of $\langle\tau\rangle$, presumably due the formation of more bulky ion clusters as opposed to linear strings (cf. Figures 5c and 5d). This suggests that the relaxation of the local surroundings is relevant for the motion of both ionic species (cf. sketch in Figure 4a).

At the same time, we observe that the diffusion coefficients of both ion species are roughly comparable for a given concentration, and decrease approximately linearly with increasing salt concentration (see Figure 16 in SI). Based on the diffusion coefficients, we obtain transport numbers similar in spirit to PFG-NMR (pulsed-field-gradient nuclear magnetic resonance) experiments, $T_+ = D_+/(D_+ + D_-)$, that are approximately $T_+ \approx 0.5$ (see SI for a more detailed discussion). Although this estimate ignores contributions from ion correlations, it suggests that both ion species are approximately equally mobile in agreement with the results from the Bruce-Vincent measurements. However, at large salt concentrations, the ratio of the cation and anion diffusion coefficient

D_+/D_- increases above unity (see Figure 17 in SI), suggesting that the lithium dynamics becomes relatively faster in this regime. Note that although the single ion dynamics apparently decreases with salt concentration, the experimentally observed increase in the conductivity can be related to the increased number of ionic charge carriers.

Figure 6b also shows the probability p_p that the LiTfSI cluster percolates throughout the entire simulation box [50] (blue curve, averaged over all time frames of the simulation). While p_p is virtually zero up to 20 wt% LiTfSI, it becomes about 43 % for 30 wt% LiTfSI and 84 % for 42 wt% LiTfSI, confirming the trends from visual inspection of Figure 5. Interestingly, also for the highest LiTfSI concentration, p_p is smaller than one due to fluctuations of the cluster shape. These fluctuations are related to significant motions of the copolymer segments, which show displacements up to one nanometer on the simulated time scale (not shown). It should be noted, however, that the center-of-mass motion of the copolymer chains is substantially slower despite their short length, such that the copolymer dynamics basically causes shape fluctuations but no net movement of the ion clusters. This is in line with the fact that we find no significant time dependence of p_p (see Figure 15 in SI). Remarkably, the fluctuations of the cluster shape and its connectivity (i.e. alternatly percolating or non-percolating) can be interpreted within the analytical Dynamic Bond Percolation model describing ion transport in amorphous polymer hosts [51].

Besides the local ion hopping dynamics, the diffusion coefficients and the network formed by the ion clusters, computation of the conductivity, including the cooperative motion of distinct ions, would provide a more complete picture. Unfortunately, these calculations would require substantially longer simulation runs. From our analysis, however, we clearly observe that in P(VdF-HFP)-LiTfSI electrolytes, the diffusion of Li^+ and $TfSI^-$ are comparable, in contrast to conventional polyether-based electrolytes (at least when sufficiently long and immobile chains are considered), in which Li^+ is significantly slower due to the strong interaction with the polymer [32, 52, 33, 53].

4. Conclusion

Films based on copolymer P(VdF-HFP) with good intrinsic properties like high temperature stability, low electron conductivity and chemical inertness were successfully modified by the addition of LiTfSI salt, resulting in significantly enhanced conductivities in the range of 10^{-5} S/cm at room temperature. The addition of LiTfSI resulted in a structural change in the crystalline parts of the semi crystalline copolymer matrix. The formation of the γ-phase of P(VdF) was confirmed by Raman spectroscopy. According to the Raman results, LiTfSI forms aggregates in the amorphous phase of the copolymer films and MD simulations show that Li^+ is coordinated by four oxygen atoms, mostly originating from distinct $TfSI^-$. The salt clusters percolate at higher salt contents. In agreement with the Arrhenius like behaviour of the conductivities in the modified films and the evaluated MD simulations, a hopping mechanism is proposed for the movement of Li^+ ions through a network of salt channels in the amorphous areas of the copolymer matrix, enabled by $TfSI^-$ stabilized sites where Li^+ is locally coordinated to oxygen atoms of the sylfonyl groups of $TfSI^-$ anions.

5. Acknowledgements

The authors wish to acknowledge the European Regional Development Fund (EFRE) and the federal state of Sachsen-Anhalt for foundation of the INZELL project, a cooperation with enspring GmbH under supervision of Robert Schlegel and the Federal Ministry of Education and Research (BMBF) for funding within the FestBatt cluster (funding number 03XP0174B). We like to thank Prof. Dr. Michael Bron and Simon Johannes Kinkelin (Martin-Luther University Halle-Wittenberg, Technical Chemistry) for providing measurement equipment and technical advices, Andy Bivour and Toni Buttlar (Martin-Luther University Halle-Wittenberg, Solid-State Chemistry) for the XRD measurements, Frank Syrowatka (Martin-Luther University Halle-Wittenberg, Interdisciplinary Center of Materials Science) for the SEM images, and Dr. Arthur Markus Anton

(Leipzig University, Peter Debye Institute for Soft Matter Physics and University of Sheffield, Department of Physics and Astronomy) for carrying out the BDS measurements at the laboratories in the work group of Prof. Dr. Friedrich Kremer (Leipzig University, Peter Debye Institute for Soft Matter Physics).

References

[1] D. Zhou, D. Shanmukaraj, A. Tkacheva, M. Armand, G. Wang, Polymer Electrolytes for Lithium-Based Batteries: Advances and Prospects, Chem (2019). doi:10.1016/j.chempr.2019.05.009.

[2] G. S. MacGlashan, Y. G. Andreev, P. G. Bruce, Structure of the polymer electrolyte poly(ethylene oxide)$_6$:LiAsF$_6$, Nature 398 (6730) (1999) 792–794. doi:10.1038/19730.

[3] C. H. Chan, H.-W. Kammer, L. H. Sim, S. N. H. M. Yusoff, A. Hashifudin, T. Winie, Conductivity and dielectric relaxation of Li salt in poly(ethylene oxide) and epoxidized natural rubber polymer electrolytes, Ionics 20 (2) (2014) 189–199. doi:10.1007/s11581-013-0961-7.

[4] C. Capiglia, Y. Saito, H. Kataoka, T. Kodama, E. Quartarone, P. Mustarelli, Structure and transport properties of polymer gel electrolytes based on PVdF-HFP and LiN($C_2F_5SO_2$)$_2$, Solid State Ionics 131 (2000) 291–299. doi:10.1016/s0167-2738(00)00678-0.

[5] W. Liu, X. K. Zhang, F. Wu, Y. Xiang, A study on PVDF-HFP gel polymer electrolyte for lithium-ion batteries, IOP Conference Series: Materials Science and Engineering 213 (2017) 012036. doi:10.1088/1757-899x/213/1/012036.

[6] X. Yan, Z. Li, Z. Wen, W. Han, Li/$Li_7La_3Zr_2O_{12}$/$LiFePO_4$ All-Solid-State Battery with Ultrathin Nanoscale Solid Electrolyte, The Journal of Physical Chemistry C 121 (3) (2017) 1431–1435. doi:10.1021/acs.jpcc.6b10268.

[7] F. Croce, L. Persi, B. Scrosati, F. Serraino-Fiory, E. Plichta, M. Hendrickson, Role of the ceramic fillers in enhancing the transport properties of composite polymer electrolytes, Electrochimica Acta 46 (16) (2001) 2457–2461. doi:10.1016/s0013-4686(01)00458-3.

[8] X. Zhang, T. Liu, S. Zhang, X. Huang, B. Xu, Y. Lin, B. Xu, L. Li, C.-W. Nan, Y. Shen, Synergistic Coupling between $Li_{6.75}La_3Zr_{1.75}Ta_{0.25}O_{12}$

and Poly(vinylidene fluoride) Induces High Ionic Conductivity, Mechanical Strength, and Thermal Stability of Solid Composite Electrolytes, Journal of the American Chemical Society 139 (39) (2017) 13779–13785. doi:10.1021/jacs.7b06364.

[9] X. Zhou, H. Jiang, H. Zheng, Y. Sun, X. Liang, H. Xiang, Nonflammable hybrid solid electrolyte membrane for a solid-state lithium battery compatible with conventional porous electrodes, Journal of Membrane Science (2020) 117820doi:10.1016/j.memsci.2020.117820.

[10] R. Gonçalves, D. Miranda, A. Almeida, M. Silva, J. Meseguer-Dueñas, J. G. Ribelles, S. Lanceros-Méndez, C. Costa, Solid polymer electrolytes based on lithium bis(trifluoromethanesulfonyl)imide/poly(vinylidene fluoride-co-hexafluoropropylene) for safer rechargeable lithium-ion batteries, Sustainable Materials and Technologies 21 (2019) e00104. doi:10.1016/j.susmat.2019.e00104.

[11] M. A. Bachmann, J. L. Koenig, Vibrational analysis of phase III of poly(vinylidene fluoride), The Journal of Chemical Physics 74 (10) (1981) 5896–5910. doi:10.1063/1.440908.

[12] A. S. Gozdz, C. N. Schmutz, J.-M. Tarascon, Rechargeable lithium intercalation battery with hybrid polymeric electrolyte, US Patent (5,296,318) (1994).

[13] S. Abbrent, J. Plestil, D. Hlavata, J. Lindgren, J. Tegenfeldt, Å. Wendsjö, Crystallinity and morphology of PVdF–HFP-based gel electrolytes, Polymer 42 (4) (2001) 1407–1416. doi:10.1016/s0032-3861(00)00517-6.

[14] Z. Stoeva, I. Martin-Litas, E. Staunton, Y. G. Andreev, P. G. Bruce, Ionic Conductivity in the Crystalline Polymer Electrolytes PEO_6:$LiXF_6$, X = P, As, Sb, Journal of the American Chemical Society 125 (15) (2003) 4619–4626. doi:10.1021/ja029326t.

[15] K. Elamin, M. Shojaatalhosseini, O. Danyliv, A. Martinelli, J. Swenson, Conduction mechanism in polymeric membranes based on PEO or PVdF-HFP and containing a piperidinium ionic liquid, Electrochimica Acta 299 (2019) 979–986. doi:10.1016/j.electacta.2018.12.154.

[16] J.-M. Tarascon, A. S. Gozdz, C. Schmutz, F. Shokoohi, P. C. Warren, Performance of Bellcore's plastic rechargable Li-ion batteries, Solid State Ionics 86-88 (1) (1996) 49–54. doi:10.1016/0167-2738(96)00330-X.

[17] S. B. Aziz, T. J. Woo, M. Kadir, H. M. Ahmed, A conceptual review on polymer electrolytes and ion transport models, Journal of Science: Advanced Materials and Devices 3 (1) (2018) 1–17. doi:10.1016/j.jsamd.2018.01.002.

[18] D. M. Seo, P. D. Boyle, R. D. Sommer, J. S. Daubert, O. Borodin, W. A. Henderson, Solvate structures and spectroscopic characterization of LiTFSI electrolytes, The Journal of Physical Chemistry B 118 (47) (2014) 13601–13608. doi:10.1021/jp505006x.

[19] Z. Li, G. Su, X. Wang, D. Gao, Micro-porous P(VDF-HFP)-based Polymer Electrolyte Filled With AlO Nanoparticles, Solid State Ionics 176 (23-24) (2005) 1903–1908. doi:10.1016/j.ssi.2005.05.006.

[20] A. M. Stephan, K. S. Nahm, M. A. Kulandainathan, G. Ravi, J. Wilson, Poly(vinylidene fluoride-hexafluoropropylene) (PVdF-HFP) based composite electrolytes for lithium batteries, European Polymer Journal 42 (8) (2006) 1728–1734. doi:10.1016/j.eurpolymj.2006.02.006.

[21] Z. Zhang, R. G. Antonio, K. L. Choy, Boron nitride enhanced polymer/salt hybrid electrolytes for all-solid-state lithium ion batteries, Journal of Power Sources 435 (2019) 226736. doi:10.1016/j.jpowsour.2019.226736.

[22] F. Kremer, A. Schönhals (Eds.), Broadband Dielectric Spectroscopy, Springer-Verlag Berlin Heidelberg GmbH, 2003.

[23] C. H. Chan, H.-W. Kammer, Impedance spectra of polymer electrolytes, Ionics 23 (9) (2017) 2327–2337. doi:10.1007/s11581-017-2174-y.

[24] C. H. Chan, H.-W. Kammer, Characterization of polymer electrolytes by dielectric response using electrochemical impedance spectroscopy, Pure and Applied Chemistry 90 (6) (2018) 939–953. doi:10.1515/pac-2017-0911.

[25] O. Borodin, Polarizable force field development and molecular dynamics simulations of ionic liquids, The Journal of Physical Chemistry B 113 (33) (2009) 11463–11478. doi:10.1021/jp905220k.

[26] D. Bedrov, J.-P. Piquemal, O. Borodin, A. D. MacKerell, B. Roux, C. Schröder, Molecular Dynamics Simulations of Ionic Liquids and Electrolytes Using Polarizable Force Fields, Chemical Reviews 119 (13) (2019) 7940–7995. doi:10.1021/acs.chemrev.8b00763.

[27] G. J. Martyna, M. L. Klein, M. Tuckerman, Nosé–Hoover chains: The canonical ensemble via continuous dynamics, The Journal of Chemical Physics 97 (4) (1992) 2635–2643. doi:10.1063/1.463940.

[28] J.-P. Ryckaert, G. Ciccotti, H. J. Berendsen, Numerical Integration of the Cartesian Equations of Motion of a System with Constraints: Molecular Dynamics of n-Alkanes, Journal of Computational Physics 23 (3) (1977) 327–341.

[29] B. J. Palmer, Direct Application of Shake to the Velocity Verlet Algorithm, Journal of Computational Physics 104 (2) (1993) 470–472. doi:10.1006/jcph.1993.1045.

[30] G. J. Martyna, D. J. Tobias, M. L. Klein, Constant pressure molecular dynamics algorithms, The Journal of Chemical Physics 101 (5) (1994) 4177–4189. doi:10.1063/1.467468.

[31] G. J. Martyna, M. E. Tuckerman, D. J. Tobias, M. L. Klein, Explicit reversible integrators for extended systems dynamics, Molecular Physics 87 (5) (1996) 1117–1157. doi:10.1080/00268979600100761.

[32] O. Borodin, G. D. Smith, Mechanism of Ion Transport in Amorphous Poly(ethylene oxide)/LiTFSI from Molecular Dynamics Simulations, Macromolecules 39 (4) (2006) 1620–1629. doi:10.1021/ma052277v.

[33] D. Diddens, A. Heuer, O. Borodin, Understanding the Lithium Transport within a Rouse-Based Model for a PEO/LiTFSI Polymer Electrolyte, Macromolecules 43 (4) (2010) 2028–2036. doi:10.1021/ma901893h.

[34] P. Martins, A. Lopes, S. Lanceros-Mendez, Electroactive phases of poly(vinylidene fluoride): Determination, processing and applications, Progress in Polymer Science 39 (4) (2014) 683–706. doi:10.1016/j.progpolymsci.2013.07.006.

[35] H. T. M. Kobayashi, K. Tashiro, Molecular Vibrations of Three Crystal Forms of Poly(venyliden fluoride), Macromolecules 8 (2) (1975) 158–171.

[36] D. Zhao, Y. Yu, J. P. Chen, Treatment of lead contaminated water by a PVDF membrane that is modified by Zirconium, Phosphate and PVA, Water Research 101 (2016) 564–573. doi:10.1016/j.watres.2016.04.078.

[37] K. Tashiro, M. Kobayashi, H. Tadokoro, Vibrational spectra and disorder-order transition of poly(venylindene fluorid) form iii, Macromolecules 14 (6) (1981) 1757–1764.

[38] T. Boccaccio, A. Bottino, G. Capannelli, P. Piaggio, Characterization of PVDF membranes by vibrational spectroscopy, Journal of Membrane Science 210 (2) (2002) 315–329. doi:10.1016/s0376-7388(02)00407-6.

[39] J. L. Nowinski, P. Lightfoot, P. G. Bruce, Structure of $LiN(CF_3SO_2)_2$, a novel salt for electrochemistry, Journal of Materials Chemistry 4 (10) (1994) 1579. doi:10.1039/jm9940401579.

[40] D. W. McOwen, D. M. Seo, O. Borodin, J. Vatamanu, P. D. Boyle, W. A. Henderson, Concentrated electrolytes: decrypting electrolyte properties

and reassessing Al corrosion mechanisms, Energy and Environmental Science 7 (1) (2014) 416–426. doi:10.1039/c3ee42351d.

[41] K. Dokko, D. Watanabe, Y. Ugata, M. L. Thomas, S. Tsuzuki, W. Shinoda, K. Hashimoto, K. Ueno, Y. Umebayashi, M. Watanabe, Direct Evidence for Li Ion Hopping Conduction in Highly Concentrated Sulfolane-Based Liquid Electrolytes, The Journal of Physical Chemistry B 122 (47) (2018) 10736–10745. doi:10.1021/acs.jpcb.8b09439.

[42] J. Mindemark, M. J. Lacey, T. Bowden, D. Brandell, Beyond PEO—alternative host materials for li $^{+}$ -conducting solid polymer electrolytes, Progress in Polymer Science 81 (2018) 114–143. doi:10.1016/j.progpolymsci.2017.12.004.

[43] R. Mishra, N. Baskaran, P. A. Ramakrishnan, K. J. Rao, Lithium ion conduction in extreme polymer in salt regime, Solid State Ionics 112 (3-4) (1998) 261–273. doi:10.1016/s0167-2738(98)00209-4.

[44] O. Borodin, G. D. Smith, W. Henderson, Li^{+} Cation Environment, Transport, and Mechanical Properties of the LiTFSI DopedN-Methyl-N-alkylpyrrolidinium^{+} TFSI^{-} Ionic Liquids, The Journal of Physical Chemistry B 110 (34) (2006) 16879–16886. doi:10.1021/jp061930t.

[45] S. Ramesh, O. P. Ling, Effect of ethylene carbonate on the ionic conduction in poly(vinylidenefluoride-hexafluoropropylene) based solid polymer electrolytes, Polymer Chemistry 1 (5) (2010) 702. doi:10.1039/b9py00244h.

[46] G. Teyssedre, C. Laurent, Charge transport modeling in insulating polymers: from molecular to macroscopic scale, IEEE Transactions on Dielectrics and Electrical Insulation 12 (5) (2005) 857–875. doi:10.1109/tdei.2005.1522182.

[47] Z. Li, G. D. Smith, D. Bedrov, Li^{+} Solvation and Transport Properties in Ionic Liquid/Lithium Salt Mixtures: A Molecular Dynamics Simulation

Study, The Journal of Physical Chemistry B 116 (42) (2012) 12801–12809. doi:10.1021/jp3052246.

[48] V. Lesch, Z. Li, D. Bedrov, O. Borodin, A. Heuer, The influence of cations on lithium ion coordination and transport in ionic liquid electrolytes: a MD simulation study, Physical Chemistry Chemical Physics 18 (1) (2016) 382–392. doi:10.1039/C5CP05111H.

[49] K. Oldiges, D. Diddens, M. Ebrahiminia, J. Hooper, I. Cekic-Laskovic, A. Heuer, D. Bedrov, M. Winter, G. Brunklaus, Understanding transport mechanisms in ionic liquid/carbonate solvent electrolyte blends, Physical Chemistry Chemical Physics 20 (24) (2018) 16579–16591. doi:10.1039/C8CP01485J.

[50] M. S. Watanabe, Percolation with a periodic boundary condition: The effect of system size for crystallization in molecular dynamics, Physical Review E 51 (5) (1995) 3945. doi:10.1103/PhysRevE.51.3945.

[51] S. D. Druger, A. Nitzan, M. A. Ratner, Dynamic bond percolation theory: A microscopic model for diffusion in dynamically disordered systems. I. Definition and one-dimensional case, The Journal of Chemical Physics 79 (6) (1983) 3133–3142. doi:10.1063/1.446144.

[52] A. Maitra, A. Heuer, Cation Transport in Polymer Electrolytes: A Microscopic Approach, Physical review letters 98 (22) (2007) 227802. doi:10.1103/PhysRevLett.98.227802.

[53] D. Diddens, A. Heuer, Lithium Ion Transport Mechanism in Ternary Polymer Electrolyte-Ionic Liquid Mixtures: A Molecular Dynamics Simulation Study, ACS Macro Letters 2 (4) (2013) 322–326. doi:10.1021/mz3006457.

[54] T. Shimanouchi, Tables of Molecular Vibrational Frequencies Consolidated Volume I, Vol. 1, National Bureau of Standards, 1972.

[55] J. Evans, C. A. Vincent, P. G. Bruce, Electrochemical measurement of transference numbers in polymer electrolytes, Polymer 28 (13) (1987) 2324–2328. doi:10.1016/0032-3861(87)90394-6.

[56] R. Buck, Diffuse layer charge relaxation at the ideally polarized electrode, Journal of Electroanalytical Chemistry and Interfacial Electrochemistry 23 (2) (1969) 219–240. doi:10.1016/s0022-0728(69)80212-3.

[57] F. Wohde, M. Balabajew, B. Roling, Li^+Transference Numbers in Liquid Electrolytes Obtained by Very-Low-Frequency Impedance Spectroscopy at Variable Electrode Distances, Journal of The Electrochemical Society 163 (5) (2016) A714–A721. doi:10.1149/2.0811605jes.

[58] P. G. Bruce, C. A. Vincent, Steady state current flow in solid binary electrolyte cells, Journal of Electroanalytical Chemistry and Interfacial Electrochemistry 225 (1-2) (1987) 1–17. doi:10.1016/0022-0728(87)80001-3.

[59] W. Zhao, F. Leroy, B. Heggen, S. Zahn, B. Kirchner, S. Balasubramanian, F. Müller-Plathe, Are There Stable Ion-Pairs in Room-Temperature Ionic Liquids? Molecular Dynamics Simulations of 1-n-Butyl-3-methylimidazolium Hexafluorophosphate, Journal of the American Chemical Society 131 (43) (2009) 15825–15833. doi:10.1021/ja906337p.

[60] J. R. Keith, S. Mogurampelly, F. Aldukhi, B. K. Wheatle, V. Ganesan, Influence of molecular weight on ion-transport properties of polymeric ionic liquids, Physical Chemistry Chemical Physics 19 (43) (2017) 29134–29145. doi:10.1039/c7cp05489k.

6. Supplementary Information

Completeness of solvent evaporation during film processing

In the Raman spectra there is no indication for residual solvent in the dried copolymer films. See Figure 7 for a detailed analysis of the bands seen in measurements of a copolymer in acetone solution and the dried copolymer films without and with 20 wt.-% LiTfSI. The vibrational frequencies for the solution are assigned in agreement with [54] and the characteristic bands of the crystalline phase seen in Raman spectra of the pure copolymer film can all be atributed to the α-phase of P(VdF) according to the detailed study of Kobayashi *et al.*[35].

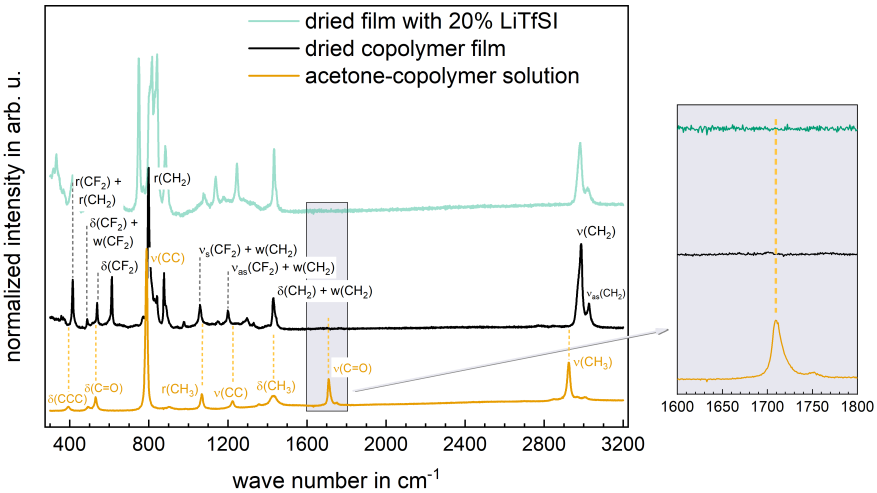

Figure 7: Raman spectra of a P(VdF-HFP)-acetone solution and a dried P(VdF-HFP) film with band assignements according to [54] and [35], respectively. The characteristic band of stretching modes of the carbonyl group in acetone is only present in the solution, while the dried films with and without salt show no bands in the specific area of $\approx$ 1600-1800 cm^{-1} (grey graph on the right). The arising bands in the pure copolymer film can all be attributed to the α-phase of P(VdF) [35].

Here we want to discuss the phenomena of the increasing conductivity seen in the P(VdF-HFP)-LiTfSI films. Additional drying procedures were tested to prove the trend is not a result of captured solvent in the films. Three samples where dried over night at 120°C and impedance measurements were performed

directly afterwards. The extracted conductivity values show a shift within the standard deviation we see, evaluating the measurements of different samples and the discussed trend is still dominating (see Figure 8).

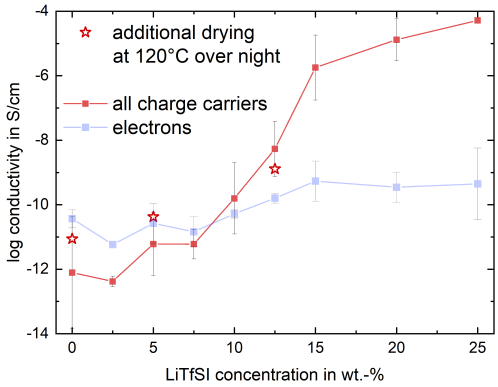

Figure 8: Conductivities evaluated from impedance and polarization measurements with the standard deviation over several measurements of different samples with same composition. The additionally heated samples show conductivities (red stars in the graph) that are within the standard deviation and the trend is not affected.

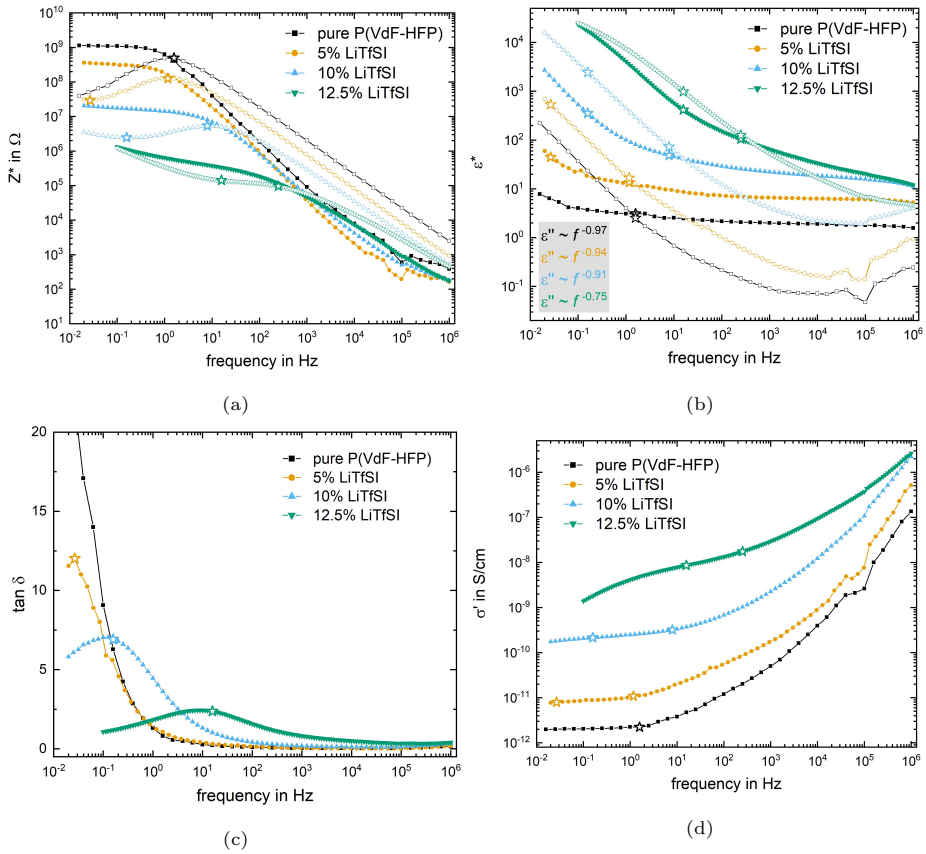

Figure 9: Frequency dependent presentation of the impedance measurements for pure copolymer and films with 5, 10, 12.5 % LiTfSI. Solid markers represent the real and empty the imaginary part of complex quantities. (a) Measured real (Z') and imaginary (Z'') part of the impedance. (b) Real (ε') and imaginary (ε'') part of the complex permittivity, (c) tangent loss spectra, and (d) real (σ') part of the complex conductivity, calculated from the measured impedance.

The impedance data are evaluated according to the dielectric spectroscopy school, using frequency dependent plots. The focus is put on relaxation phenomena strongly depending on the applied frequency [22]. Not only complex impedance, but also the closely related permittivity and conductivity in the measured frequency range is considered for the evaluation.

Set under an alternating voltage between two ion blocking electrodes, the sample forms a parallel plate capacitor with area A and thickness l and the complex capacitance is given by

$$C^* = \varepsilon^* C_0 = \varepsilon^* \varepsilon_0 \frac{A}{l}$$

While $\varepsilon_0 = 8.854 \cdot 10^{-12}$ As/Vm is the permittivity of vacuum, the complex permittivity ε^* is related to impedance Z^* in the linear range by

$$Z^* = Z' + iZ'' = \frac{1}{C^*} = \frac{1}{i\omega C_0 \varepsilon^*}$$

with angular frequency $\omega = 2\pi f$. The real and imaginary part of the permittivity is then given by

$$\varepsilon' = \frac{l}{A\omega\varepsilon_0} \cdot \frac{Z''}{|Z|^2} \text{ and } \varepsilon'' = \frac{l}{A\omega\varepsilon_0} \cdot \frac{Z'}{|Z|^2}$$

The permittivity is closely related to complex conductivity, according to the following correlation

$$\sigma^* = i\omega\varepsilon_0\varepsilon^*$$

and the division into real and complex part of the conductivity leads to

$$\sigma' = \frac{l}{A}\frac{Z'}{|Z|^2} \text{ and } \sigma'' = \frac{l}{A}\frac{Z''}{|Z|^2}$$

The impedance data here are analysed according to the detailed describtion of Chan *et al.* [3, 23, 24].

In Figure 9a real and imaginary part of the impedance (Z' and Z'') are plotted versus the applied frequency in a double logarithmic plot for pure copolymer and copolymer films with 5, 10 and 12.5 wt.-% LiTfSI. For pure P(VdF-HFP) and low salt concentration of 5 wt.-% the real and imaginary part of the complex impedance show a similar course, while higher salt concentrations lead to a electrode polarization that is dominating the low frequency range.

Z' reaches a steady resistance value at low frequencies and Z'' a maxima close to the crossing point of Z' and Z''. For higher frequencies $Z'' > Z'$, and Z'' shows a monotone increase.

The local maximum in Z'' (f_{max}, indicated in Figure 9a with stars) results from

a relaxation process. For higher salt concentration this maximum shifts towards higher frequencies and there is a local minimum (indicated by a star in Figure 9a) with $f_{min} < f_{max}$ indicating the onset of the development of a double layer at the electrode-electrolyte interface (polarization of the electrodes). For high salt concentrations Z' and Z'' show a monotone increase at frequencies $< f_{min}$, that is dominating the investigated frequency range, resulting from the strong polarization of the electrodes. Beside f_{min} and f_{max}, the crossing of Z' and Z'' (f_{cross}) gives another important point in the graphs. For $f_{max} = f_{cross}$ the relaxation process is an ideal Debye relaxation with one relaxation constant τ. In our measurements we see $f_{max} < f_{cross}$ revealing a slight deviation from Debye behaviour. Z', representing ohmic resistance reaches a constant value in the low frequency range. With increasing salt concentration the hight of the Z' plateau is strongly decreasing showing the reduced ohmic resistance of the copolymer films. In Figure 9b real and imaginary part of the complex permittivity are plotted against the frequency, ε' indicating the ability of the material to store energy and ε'' representing dielectric loss. Dissipation of energy in the polymer films can be due to dipole migration, flow of charged entities or conversion into thermal energy, like molecular vibration. In the frequency range $f_{min}^{Z''} < f < f_{max}^{Z''}$ the graph (characteristic frequencies are marked with stars) shows a linear course in the double logarithmic plot and $\varepsilon'' \propto \omega^{-n}$ (or $\varepsilon'' \propto f^n$), with n = 1 for processes following the Debye relaxation and n < 1, but close to unity for slight deviations from the ideal Debye relaxation. For our samples we get values of n = 0.97, 0.94, 0.91, 0.75 for 0, 5, 10 and 12.5 wt.% LiTfSI, respectively. This shows the continuously increase of deviation from Debye relaxation with increasing salt concentration. Figure 9c shows the tangent loss spectra for the four samples. It can clearly be seen, that for higher salt concentration there is a energy loss due to electrode polarization in the middle of the analysed frequency range. The slight mismatch $f_{max}^{\delta} \neq f_{min}^{Z''}$ shows the deviation from Debye relaxation again. The frequency values for the maxima in $\tan(\delta)$ are shifting towards higher frequencies for increasing salt concentration.

The real part of the complex conductivity (σ') is a measure for the flow of

charges, while σ'' reflects the storage of charge. Plotting the real part of the conductivity σ' against the frequency f in a double logarithmic plot (see Figure 9d), the so called DC-conductivity (σ_{DC}) of the samples can be extracted. The real part of the conductivity $\sigma' \propto \varepsilon''\omega$ and $\varepsilon'' \propto \omega^{-n}$, leads to $\sigma' \propto \omega^{1-n}$, with $n < 1$, but close to unity we expect $\sigma' \approx$constant in the low frequency range $f_{min}^{Z''} < f < f_{max}^{Z''}$. Due to deviation from Debye relaxation, the conductivity still shows small frequency dependence, but still extrapolation to smaller frequencies yields $\sigma'(0) = \sigma DC$. For high salt concentrations polarization is dominating the small frequency range and σ' is strongly decreasing at frequencies smaller than $f_{min}^{Z''}$.

The extracted conductivity is the over all conductivity of the sample including any charged carrier moving within the copolymer film. Regardless of the variation between evaluated measurements of samples with the same salt concentration, the trend in the concentration series is very clear. The addition of salt strongly increases the conductivity of the copolymer films.

Transference / transport numbers

Transference numbers are a measure for the contribution of specific charge carriers to the total current in an electrolyte material. In polymer-salt systems with mobile lithium cations and the corresponding movable salt anions, Bruce-Vincent (BV) measurements [55] are often used to determine the cationic transference number, combining AC and DC methods. The initial and the steady state resistance (R_0, R_s) of the cell are measured via impedance, while a polarization experiment of the electrolyte layer between Lithium metal electrodes (set under a small potential) yields the initial and steady state current (I_0, I_s). The salt is thought to be dissolved in isolated ions that are stabalized through interactions with the surrounding media (e.g. polymer chains, solvent). For small polarizations ($\Delta V = 10\,\mathrm{mV}$) and neglecting ion-ion interactions I_0

and I_s are defined as follows [55]

$$I_0 = \frac{\Delta V}{R_1^0 + R_2} = \frac{\Delta V}{R_1^0 + k/\sigma}$$

and

$$I_s = \frac{\Delta V}{R_1^s + k/(t_+ \cdot \sigma)}$$

With ΔV being the applied potential, R_1 the resistance of the passivation layer that forms at the electrode during the polarization, R_2 and σ the resistance and dc conductivity of the electrolyte, k the cell constant and t_+ the transference number for cations. Combination of the two equations leads to

$$t_+ = \frac{I_s \cdot (\Delta V - I_0 R_1^0)}{I_0 \cdot (\Delta V - I_s R_1^s)}$$

Another method is the estimation of t_+ from diffusion coefficients (D_+ and D_- for cations and anions, respectively) [56], that could be measured with PFG-NMR. This approach does not take into account ion-ion-interaction and consideres an ideal system with independent migration of anions and cations. Here we compare the results from Bruce-Vincent measurements with t_+ calculated from the diffusion coefficients extracted from the MD simulations. Although MD simulations in principle also allow the determination of ionic conductivities, these quantities require substantially larger amounts of simulation data, and were hence not calculated within the present work. It should be stressed that transference numbers determined by the Bruce-Vincent method contain contributions from the correlated motion of ions, thus reflecting the fraction of *charge* transported by the individual ion species, while estimates from the ionic diffusion coefficients ignore these contributions, and thus measure the fraction of *mass* or *ions* transported by either species. The latter one is referred to as transport number for cations T_+ [57] to distinguish between the two different approaches.

A sample with a salt content of 12.5 wt.-% LiTfSI was measured between lithium metal electrodes in a Swagelok cell. The cell was assembled in a nitrogen filled glove-box with oxygen levels kept below 1 ppm. The airtight sealed

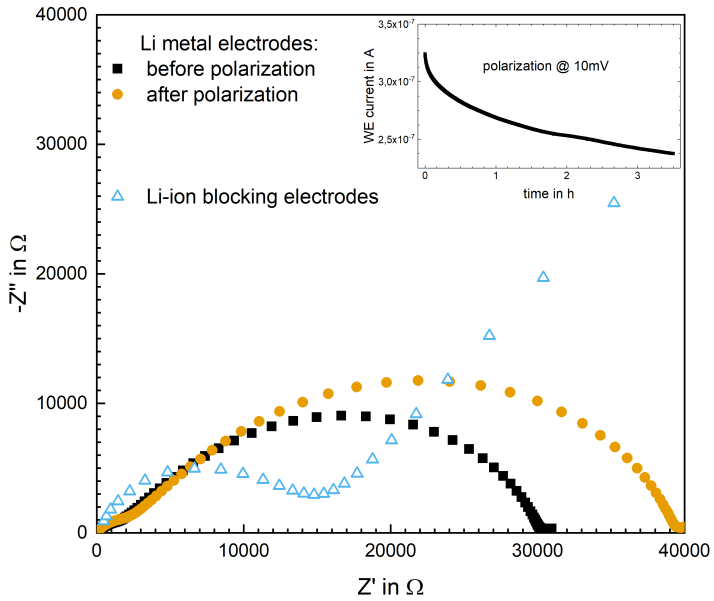

Figure 10: Impedance plots and current development over time during the polarization of Bruce-Vincent-measurements of a copolymer film with 12.5 wt.-% LiTfSI measured between lithium metal electrodes (solid markers) and impedance measurement between stainless steel lithium ion blocking electrodes (open markers). The Bruce-Vincent measurement gave a t_{Li^+} of 0.47 (see table 1 for more details).

cell was taken out of the glove-box and connected to a Metrohm Autolab PGSTAT128N potentiostat equipped with an additional impedance analyzer and Autolab Nova software. Impedance measurements (10^6-10^{-2} Hz, 10 mV amplitude) were performed before and after the polarization with a potential of 10 mV. The measurements are shown in Figure 10, extracted date are summarized in Table 1. The measurements gave a t_{Li^+} of 0.47.

R_0 in Ω	R_s in Ω	I_0 in A	I_s in A	ΔU in V	t_{Li^+}
$3.0{\cdot}10^4$	$3.9{\cdot}10^4$	$3.2{\cdot}10^{-7}$	$2.4{\cdot}10^{-7}$	$1.0{\cdot}10^{-2}$	0.47

Table 1: Extracted values from Bruce-Vincent measurements

Figure 17 shows the fraction of D_{Li^+}/D_{TfSI^-} and the calculated transport numbers according to

$$T_{Li^+} = \frac{D_{Li^+}}{D_{Li^+} + D_{TfSI^-}}$$

for the four simulated concentrations as extracted from the MD simulations (note however that the simulations were performed at a slightly larger temperature of $T = 363\,\mathrm{K}$). The calculated transport numbers of ≈ 0.5 are in good agreement with the measured t_{Li^+} from Bruce-Vincent measurements indicating a comparable mobility of Li^+ and $TfSI^-$. However, D_{Li^+}/D_{TfSI^-} is larger than one for higher concentrations, suggesting that Li^+ diffuses faster than the anion when there is more salt in the matrix that forms channels and provides pathways for lithium ions. This is in good agreement with the transport mechanism via hopping for lithium ions [41], which we propose here (Figure 4a).

As pointed out above, transference numbers derived from the Bruce-Vincent method and transport numbers from diffusion coefficients are conceptually different, as the former measures the fraction of transported ionic current, while the latter measures the fraction of transported particles and thus only yields correct estimates of cationic transference number when no ion-ion interactions are present. Furthermore, the derivation of the equations employed in the analysis of the Bruce-Vincent measurements relies on the assumption of negligible ion-ion interactions, or, put differently, spatially invariant transport coefficients [58], which is not strictly valid for the herein investigated material system and due to the fact that concentration gradients occur in the steady state. However, in the limit of low voltages as in our case, this assumption is usually justified [58]. Based on our findings, we assume that Li^+ cations are locally stabilized through the coordination of oxygen atoms of the TfSI anion and the proposed conduction mechanism is based on this ion-ion interaction. In this context, the measured and simulated t_{Li^+} and T_{Li^+} strongly suggest that lithium contribution plays an important role in the conduction mechanism in the discussed system. The value of 0.47 is in the range of reported lithium ion transference

numbers of different polymer-LiTfSI systems in the review of Mindemark *et al.* [42]. In coordinating polymers the lithium ion is often strongly bound to the polymer chains, reducing the cationic mobility, leading to low t_{Li^+}. Understanding the transport mechanism for lithium ions in the non-coordinating polymer P(VDF-HFP) is crucial for further investigations.

MD simulation - additional data

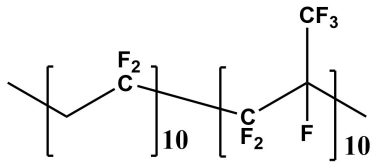

Figure 11: Structure of the simulated P(VdF-HFP) polymer chains.

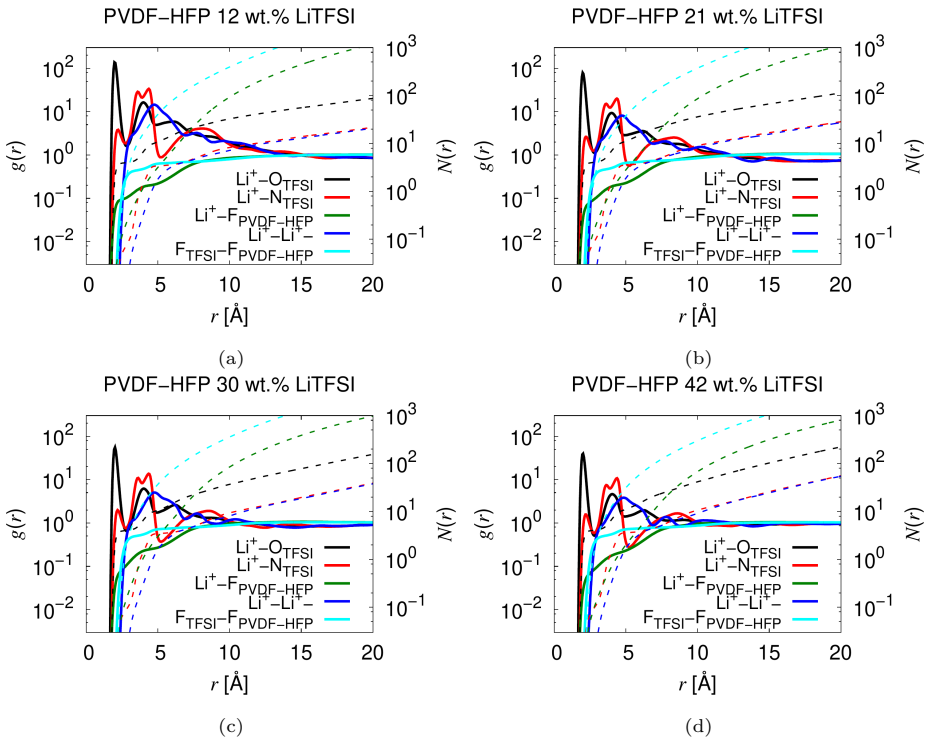

Figure 12: Radial distribution functions (RDFs) for Li^+-O_{TfSI}, Li^+-N_{TfSI}, and Li^+-N_{TfSI}. The position of the first minimum after the first coordination peak defines the spatial extension of the first coordination shell.

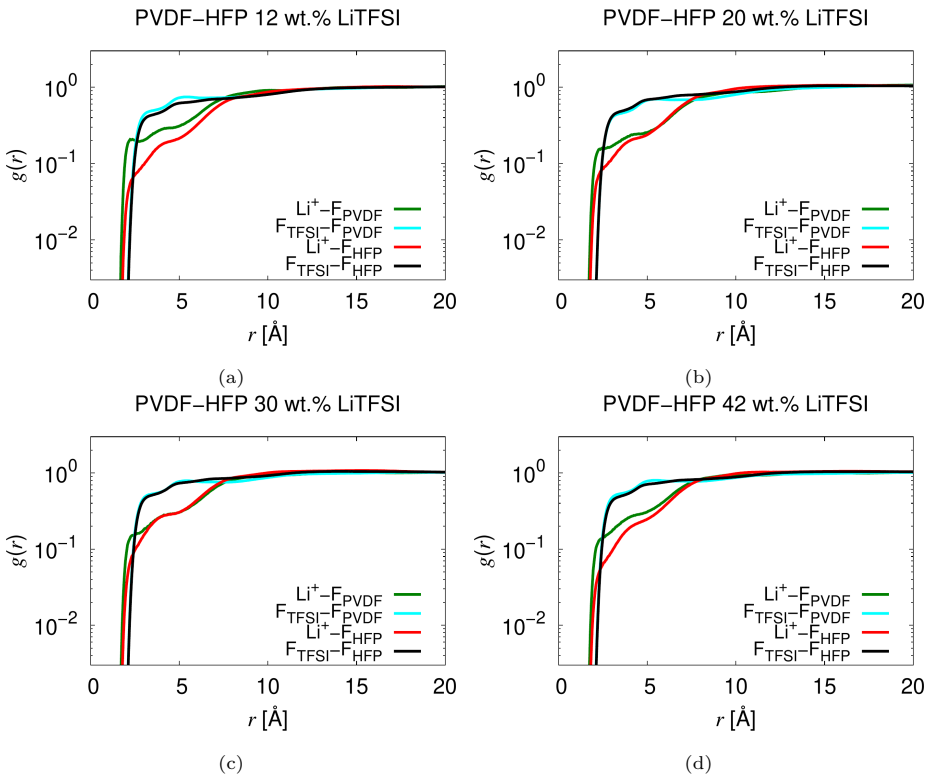

Figure 13: Radial distribution functions (RDFs) between Li^+ and fluorine atoms of PVdF and PHFP as well as between fluorine atoms of TfSI and fluorine atoms of PVdF and PHFP.

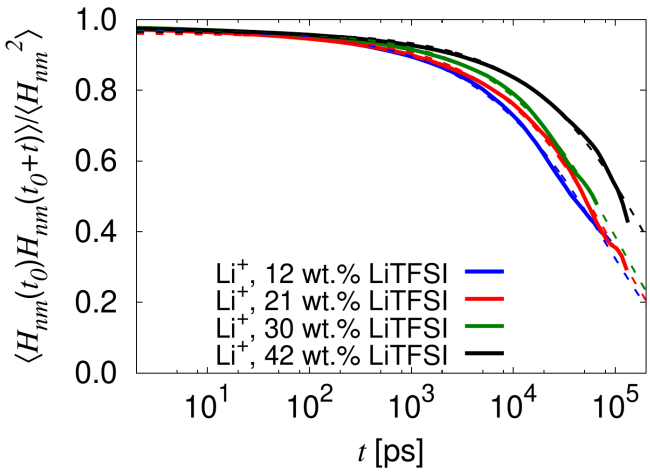

Figure 14: Normalized coordination autocorrelation functions $\langle H_{nm}(t_0)H_{nm}(t_0+t)\rangle/\langle H_{nm}^2\rangle$ as a function of time. The dashed lines indicate the fits according to Eq. 1.

To determined the average coordination lifetimes, we defined the function $H_{nm}(t_0)$ that is one if ions n and m are coordinated at starting time t_0 (as determined from Figure 12) and zero otherwise, and calculated the correlation function $\langle H_{nm}(t_0)H_{nm}(t_0+t)\rangle/\langle H_{nm}^2\rangle$ [59, 48, 60] (Figure 14). Note that events in which the ion pair is broken and reformed during t also contribute to $\langle H_{nm}(t_0)H_{nm}(t_0+t)\rangle$. Subsequently, the curves were fitted with a stretched exponential

$$\frac{\langle H_{nm}(t_0)H_{nm}(t_0+t)\rangle}{\langle H_{nm}^2\rangle} = \exp\left(-\left(\frac{t}{\tau}\right)^{\beta}\right) \tag{1}$$

and the average relaxation times $\langle\tau\rangle$ were estimated from the fits according to

$$\langle\tau\rangle = \beta^{-1}\Gamma(\beta^{-1})\,\tau \tag{2}$$

(with $\Gamma(x) = \int_0^\infty dt\, t^{x-1}\exp(-t)$ being the gamma function). The results are shown in Figure 6 in the main text.

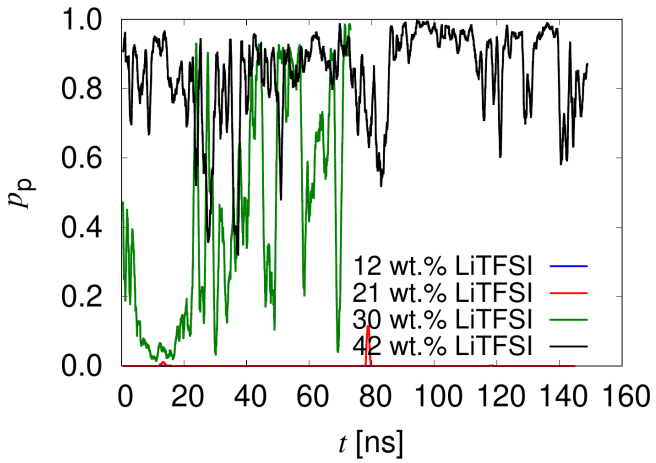

Figure 15: Time-depend percolation probability p_p as determined from a 1 ns running average over the percolation probabilities of the individual time frames of the simulations.

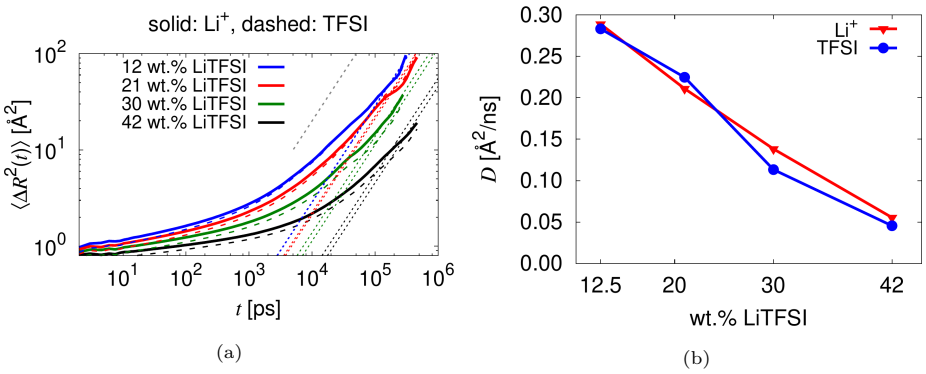

Figure 16: (a) Mean squared displacements (MSDs) of Li^+ and TfSI for the different concentrations and (b) diffusion coefficients fitted from (a). The gray dashed line in (a) indicates the linear diffusive regime, showing that the MSDs approximately become diffusive within the simulated time scale. The fits in (a) are indicated as colored dotted lines.

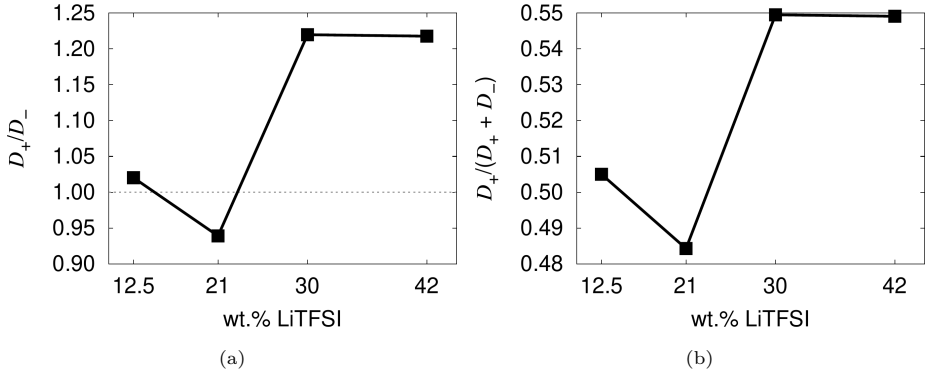

Figure 17: (a) Ratio of the cation and anion diffusion coefficient for the different concentrations. The transference number based on the diffusion coefficients in Figure 16 when ion correlations are neglected is also shown in (b) for convenience.